IVYSPRING INTERNATIONAL PUBLISHER

Theranostics

2027; 17(1): 589-603. doi: 10.7150/thno.139788

Research Paper

Bidirectional ROS cascade amplification in a TME-activatable nanoplatform for MRI-guided sono-chemodynamic cancer therapy

Linrong Shi[1,2], Chenhui He[1], Zhezhu Nan[1], Yang Liu[1], Jiayue Li[1], Mingxi Wan[1], Ping Li[3], and Yi Feng[1]✉

1. The Key Laboratory of Biomedical Information Engineering of Ministry of Education, Department of Biomedical Engineering, School of Life Science and Technology, Xi'an Jiaotong University, Xi'an 710049, China.
2. Department of Diagnostic Radiology, Yong Loo Lin School of Medicine, National University of Singapore, Singapore, 119074, Singapore.
3. MOE Key Laboratory of Thermo-Fluid Science and Engineering, Xi'an Jiaotong University, Xi'an, Shaanxi, 710049, China.

✉ Corresponding author: Yi Feng, Email: fengyi@mail.xjtu.edu.cn.

© 2027 The Author(s). This is an open access article distributed under the Creative Commons Attribution 4.0 International Licence, subject to the Publisher's Terms of Use at https://ivyspring.com/terms.

Received: 2026.06.24; Accepted: 2026.10.20; Published: 2027.01.01

Abstract

Rationale: Sono-chemodynamic therapy has emerged as a promising strategy for cancer treatment, yet most existing systems treat sonodynamic therapy (SDT) and chemodynamic therapy (CDT) as simple combined modalities, leaving their bidirectional kinetic interplay and molecular regulatory mechanisms largely unexplored.

Methods: We report a tumor microenvironment (TME)-activatable magnetic resonance imaging (MRI)-guided theranostic nanoplatform, ZMPF, constructed from a ZIF-8 sonosensitizer framework, MnO_2 catalytic decoration, and folic acid-mediated targeting. ZMPF enables the first systematic elucidation of bidirectional SDT/CDT coupling.

Results: For SDT, under ultrasound (US) treatment, ZMPF mainly generates $O_2^{\bullet-}$ (14.1-fold) over the other ROS (2.8-fold for •OH and 2.4-fold for $^1O_2$). Interestingly, for synergistic SDT and CDT under acidic H_2O_2 conditions, ZMPF achieves a 54.6-fold enhancement of $O_2^{\bullet-}$ generation, markedly exceeding SDT alone (14.9-fold) and CDT alone (28.5-fold), thereby demonstrating synergistic ROS cascade amplification beyond simple additivity. Meanwhile, GSH-triggered MnO_2 reduction activates T_1-weighted MRI with a high longitudinal relaxivity (r_1 = 6.24 mM^{-1} s^{-1}) and 1.66-fold signal increase for real-time tumor tracking. Mechanistically, RNA sequencing reveals that ZMPF-mediated sono-chemodynamic therapy alters gene expression related to oxidative stress, apoptotic signaling, and growth regulation in 4T1 cells. ZMPF+US induces pronounced apoptosis and achieves 99.2% tumor inhibition *in vivo* with excellent biosafety.

Conclusions: This work establishes ZMPF as a mechanistically informed platform for MRI-guided precision sono-chemodynamic therapy and provides a design paradigm for bidirectionally amplified SDT/CDT in tumor therapy.

Keywords: ultrasound, nanomedicine, sonodynamic therapy, chemodynamic therapy, magnetic resonance imaging

Introduction

Ultrasound (US), owing to its deep tissue penetration, spatiotemporal controllability, and non-invasiveness, has been widely used in biomedical applications [1]. Sonodynamic therapy (SDT) employs US to activate sonosensitizers for generating cytotoxic reactive oxygen species (ROS) for the treatment of deep-seated tumors [2]. Nevertheless, the ROS yield of existing SDT systems is fundamentally constrained by insufficient sonosensitizer catalytic activity and hypoxic tumor microenvironment (TME), resulting in unsatisfactory antitumor efficacy when SDT is used alone [3-5]. To address these issues, oxygen-supplying or oxygen-generating components have been introduced in SDT to alleviate hypoxia, including glucose oxidase-based nanomaterials, perfluorocarbon carriers, metal-based nanoparticles, *etc.* [6-20]. Among them, chemodynamic activity easily exploits the acidic environment and endogenous H_2O_2 within tumors to undergo Fenton or Fenton-like reactions, thereby yielding ROS and O_2 which can enhance therapeutic efficacy in SDT [21-24]. Therefore, integrating chemodynamic therapy (CDT) with SDT

represents an effective sono-chemodynamic therapeutic strategy to enhance ROS production and improve antitumor efficacy [25].

Despite growing interest in sono-chemodynamic therapy, current studies primarily regard CDT only as a supplementary modality to SDT, with their dynamic interplay largely overlooked. While US can drive chemical processes *via* cavitation, its capacity to modulate CDT catalysis remains poorly defined [26-27]. More critically, whether the integrated system achieves genuine synergistic ROS amplification beyond additive effects is still unresolved. Existing studies are mainly limited to phenotypic outcomes, lacking mechanistic insights into how SDT-CDT coupling regulates genes involved in oxidative stress, apoptotic signaling, and growth regulation at the transcriptomic level [22, 28-29]. Therefore, elucidating the bidirectional kinetic interplay between SDT and CDT under US as the primary driving force, along with its molecular regulatory mechanisms, constitutes an essential prerequisite for designing sono-chemodynamic therapeutic systems that truly transcend simple additive effects.

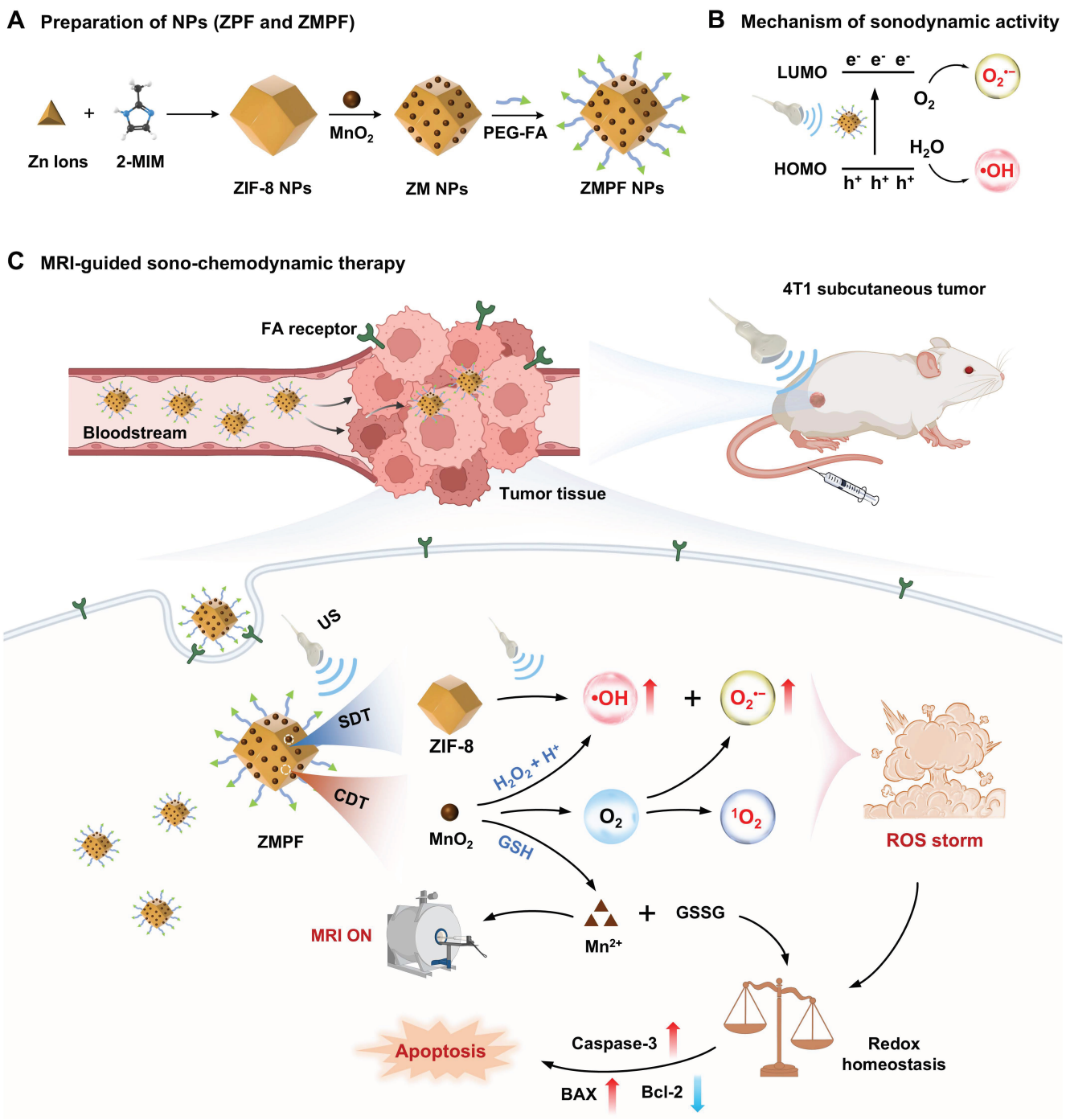
However, maximizing the aforementioned therapeutic efficacy further depends on real-time monitoring of nanoplatform accumulation status within tumors and precise identification of the optimal therapeutic window [30-32]. Conventional optical imaging, although widely used, is fundamentally limited by poor tissue penetration, restricting its application in deep-tissue visualization [33-36]. In contrast, magnetic resonance imaging (MRI), with its depth-independent penetration and excellent soft-tissue contrast, offers a superior modality for noninvasive imaging of deep-seated tumors [37-43]. However, clinically available MRI contrast agents remain in a persistent "always-on" state, generating non-specific background signals that compromise signal-to-noise ratios and preclude dynamic reporting of the activation state of therapeutic nanoplatforms in tumor [39, 44-46]. Accordingly, developing a TME-activatable MRI system that guides the precise implementation of sono-chemodynamic therapy remains challenging in practical application.

Herein, we report a TME-activatable theranostic nanoplatform, designated ZMPF, which integrates SDT, CDT, and "off-on" MRI guidance within a single nanosystem. This platform is constructed on a ZIF-8 sonosensitizer core surface-decorated with MnO_2 and functionalized with polyethylene glycol-folic acid (PEG-FA). Within the acidic, H_2O_2-enriched TME, MnO_2 drives Fenton-like CDT to generate •OH. Simultaneously, glutathione (GSH) triggers the reduction of MnO_2 to release Mn^{2+}, turning on T_1-weighted MRI contrast (r_1 = 6.24 mM^{-1} s^{-1}) for tracking real-time tumor accumulation and therapeutic response. PEG modification imparts colloidal stability and shields the ZIF-8 framework from premature acid-mediated degradation during systemic circulation, while FA mediates active tumor targeting [47]. Building upon this platform, we provide the first systematic demonstration of bidirectional kinetic interplay between SDT and CDT: US irradiation markedly accelerates the ROS generation kinetics of CDT-mediated reactions, with ROS output within 1 min surpassed that of standalone CDT at 5 min. At pH 5.5, the combined treatment increased $O_2^{\bullet-}$ generation by 54.6-fold. This increase substantially exceeded the sum of those produced by SDT alone (14.9-fold) and CDT alone (28.5-fold), indicating synergistic amplification beyond simple additivity. The resulting intensified cascading ROS storm promoted apoptosis in 4T1 breast cancer cells. Transcriptomic RNA sequencing further reveals the cooperative therapeutic mechanism at the molecular level, confirming that upregulated oxidative stress, activated apoptotic signaling pathways, and changes in growth-related gene expression collectively mediate the therapeutic outcome. Ultimately, a tumor inhibition rate of 99.2% is achieved with excellent biosafety *in vivo*. This work provides a systematic design paradigm and mechanistic basis for constructing imaging-guided and US-driven sono-chemodynamic tumor nanomedicine with bidirectionally enhanced reaction kinetics.

Results and Discussion

Preparation and characterization of ZMPF

ZPF and ZMPF were prepared as outlined in Scheme 1A. Briefly, ZIF-8 was first synthesized through the coordination reaction between 2-methylimidazole (2-MI) and $Zn(NO_3)_2$ [13, 48]. Subsequently, MnO_2 was fabricated onto ZIF-8 by the redox reaction between $MnSO_4$ and $KMnO_4$ in aqueous medium, followed by surface modification with polyethylene glycol-folic acid (PEG-FA) to yield ZIF-8@MnO_2-PEG-FA (denoted as ZMPF). As a control, PEG-FA was directly modified on ZIF-8 to produce ZIF-8-PEG-FA (termed as ZPF). Thus, ZMPF comprised ZIF-8, MnO_2 decoration and PEG-FA chains, whereas ZPF only contained ZIF-8 and PEG-FA chains (Figure 1A).



Scheme 1. Schematic illustration of the design and theranostic mechanism of the multifunctional nanoplatform ZIF-8@MnO_2-PEG-FA for sono-chemodynamic therapy. (A) Synthetic route of sonosensitizers ZPF and ZMPF NPs. (B) Mechanism of sonodynamic activity of ZMPF. (C) Schematic diagram of MRI-guided sonodynamic and chemodynamic therapy.

The physicochemical properties of ZPF and ZMPF were then examined. Both ZPF and ZMPF showed a characteristic absorption band at 210 nm arising from the ZIF-8 framework, and an additional strong and broad band at 280-400 nm attributed to MnO_2 was only observed in ZMPF (Figure S1). Then, the hydrodynamic diameters measured by dynamic light scattering (DLS) were 106 nm for ZPF and 122 nm for ZMPF, with the size increase ascribed to MnO_2 decoration (Figure 1B-C). Transmission electron microscopy (TEM) images showed uniform dodecahedral-like morphology with smaller particle sizes of ~ 90 nm (ZPF) and ~ 105 nm (ZMPF), consistent with DLS data. Moreover, TEM energy dispersive X-ray (EDX) mapping disclosed elemental distribution in both ZPF and ZMPF (Figure 1D). Notably, Mn signals were clearly detected in ZMPF but negligible in ZPF, further validated by EDS spectra

(Figure S2). X-ray photoelectron spectroscopy (XPS) was further used to examine the chemical states of Zn and Mn in ZMPF (Figure S3). The Zn $2p_{3/2}$ and Zn $2p_{1/2}$ peaks at 1021.15 and 1044.23 eV were assigned to Zn^{2+} in ZIF-8. The Mn $2p_{3/2}$ and Mn $2p_{1/2}$ peaks at 641.31 and 653.10 eV were consistent with Mn^{4+} in MnO_2, supporting the successful MnO_2 modification of ZIF-8. Then, the crystal structures of ZPF and ZMPF was examined by X-ray diffraction (XRD). Both ZPF and ZMPF showed diffraction peaks (2θ = 7.4°, 18.0°, 12.7°, 10.4°, 16.4°, and 14.7°), corresponding to the (011), (222), (112), (002), (013) and (022) planes of ZIF-8 (Figure 1E), respectively, consistent with the simulated sodalite-type cubic structure ($I\bar{4}3m$ space group) (Figure S4). However, the absence of distinct MnO_2 peaks in ZMPF was attributed to its low content and weak crystallinity. Fourier transform infrared (FT-IR) spectroscopy further verified the composition of ZPF and ZMPF. Both ZPF and ZMPF showed characteristic ZIF-8 bands at ~ 420 cm^{-1} (Zn-N stretching), 1140-1170 cm^{-1} (C-N stretching of the imidazole ring) and 1420-1460 cm^{-1} (C=N stretching), characteristic PEG-FA peaks at 1700-1725 cm^{-1} (C=O stretching of folic acid), 3300-3500 cm^{-1} (N-H stretching of -NH_2 groups) and 1100-1140 cm^{-1} (symmetric C-O-C stretching of PEG). ZMPF additionally showed a band between 500 and 650 cm^{-1}, corresponding to the Mn-O stretching vibration of MnO_2 decoration (Figure 1F). Moreover, ZMPF showed no size change for 24 h incubation, demonstrating excellent colloidal stability for further application (Figure 1G) [49]. All these data confirmed the successful synthesis of ZPF and ZMPF.

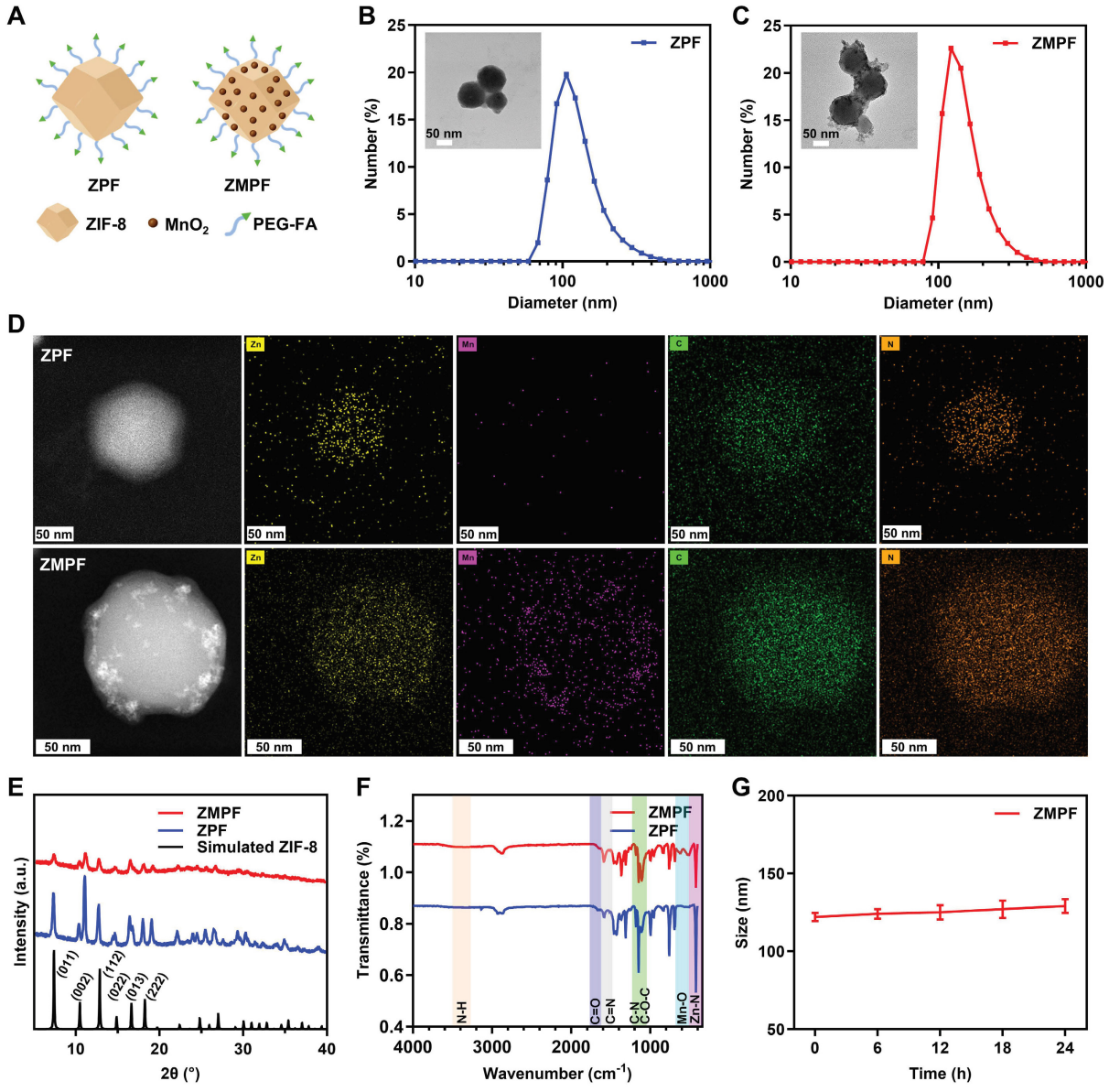


Figure 1. Fabrication and characterization of ZPF and ZMPF. (A) Schematic illustration of ZPF and ZMPF. DLS of ZPF (B) and ZMPF (C) with the corresponding TEM image as the inset (scale bar = 50 nm). Elemental mapping images (D), XRD patterns (E), and FTIR spectra (F) of ZPF and ZMPF. (G) Stability of ZMPF in deionized (DI) water evaluated by DLS at 0, 6, 12, 18 and 24 h (n = 3, mean ± s.d.).

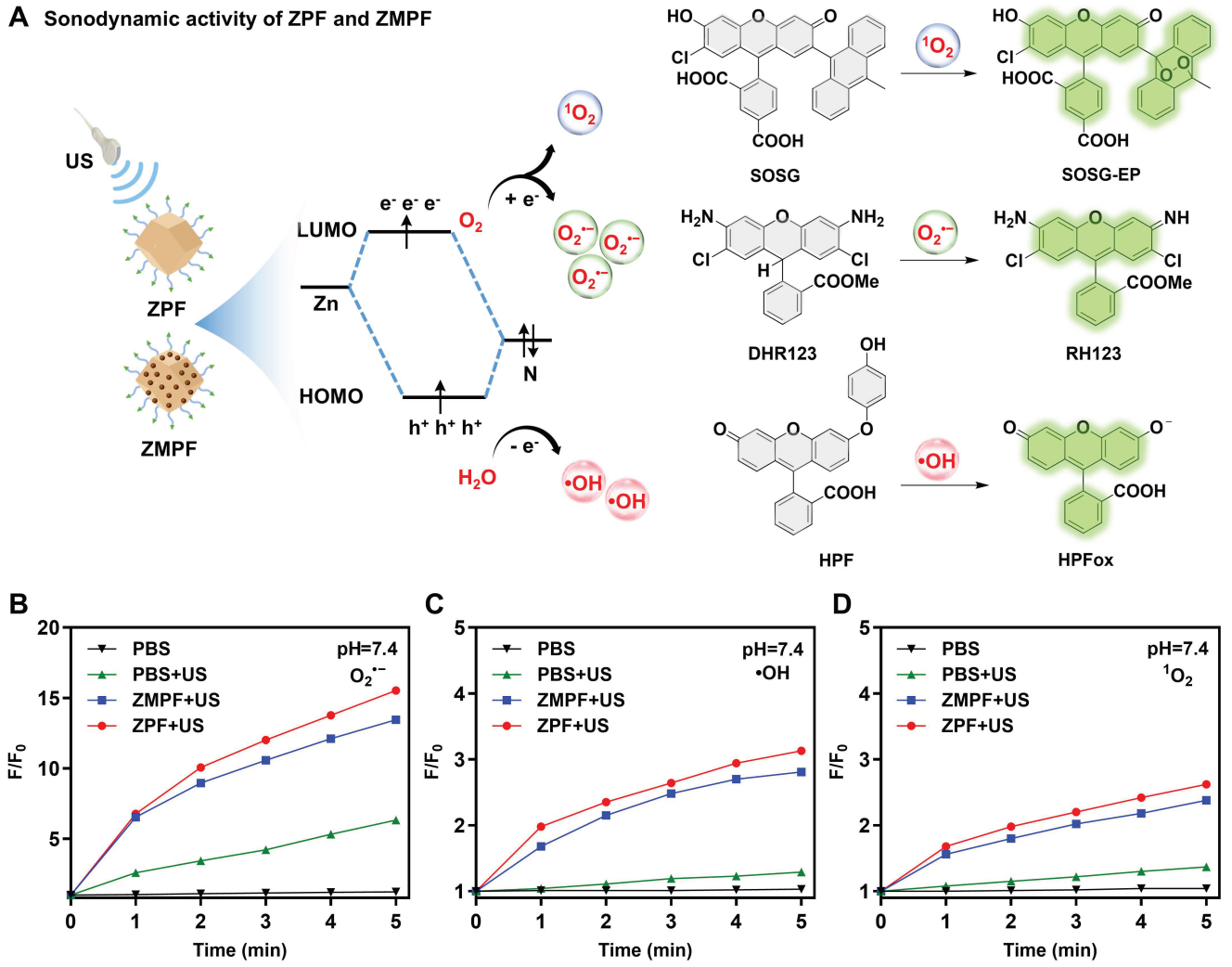


Figure 2. Evaluation of US-triggered sonodynamic ROS generation by ZPF and ZMPF. (A) Schematic illustration of ROS generation mechanism of ZMPF and ZPF upon ultrasound (US) irradiation. ROS generation of $O_2^{\bullet-}$ (B), •OH (C) and $^1O_2$ (D) from ZPF+US, ZMPF+US, PBS+US and PBS in 10 mM PBS (pH 7.4, 37 °C), respectively. F/F_0 represented the fluorescence intensity ratio of DHR123, HPF, SOSG before and after the US treatment (1.5 W cm^{-2}, 40% duty cycle) as a function of different treatment times, respectively, indicating the relative ROS generation efficiency.

In vitro sonodynamic performance

To explore sonodynamic activity of ZPF and ZMPF, their ROS generation was evaluated and compared. ROS fluorescence probes DHR123, HPF and SOSG were used to detect $O_2^{\bullet-}$, •OH and $^1O_2$ generation, respectively (Figure 2A). Under US irradiation, the unsaturated Zn-N active sites exposed on the (011) plane from ZPF and ZMPF could play a critical role in activating adsorbed O_2 and H_2O molecules to generate ROS through electron and energy transfer processes [13, 50]. As shown in Figure 2B-D, ZPF+US and ZMPF+US produced similar levels of $O_2^{\bullet-}$, •OH and $^1O_2$ at pH = 7.4, respectively. Specifically, the two groups generated the highest levels of $O_2^{\bullet-}$, with 15.5- and 14.1-fold increases, followed by •OH (3.1- and 2.8-fold) and $^1O_2$ (2.6- and 2.4-fold), respectively. These results indicated that the sonodynamic activity of ZMPF mainly originated from ZIF-8 which acted as the sonosensitizer. In addition, similar ROS generation was observed for ZPF+US and ZMPF+US at pH 6.5 and 5.5 compared with that at pH 7.4 (Figure S5), probably because the ZIF-8 was protected from acid-induced degradation by PEG chain.

In vitro sono-chemodynamic activity

Beyond evaluating sonodynamic properties of ZPF and ZMPF, their chemodynamic activities were further investigated. ZMPF consisted of ZIF-8 decorated with MnO_2 and modified with PEG-FA, whereas ZPF contained only ZIF-8 and PEG-FA. As illustrated in Figure 3A, loaded MnO_2 in ZMPF can react with endogenous H_2O_2 in TME to produce •OH through a Fenton-like route, and simultaneously generate dissolved O_2 that enhances the yields of $O_2^{\bullet-}$ and $^1O_2$ during sonodynamic process [51]. At pH 7.4, the ZMPF+H_2O_2+US group showed no detectable

increase in ROS compared with ZMPF+US (Figure 3B, E and H), demonstrating that chemodynamic activity was significantly suppressed under the neutral conditions. In contrast, ZMPF+H_2O_2+US produced markedly higher levels of $O_2^{\bullet-}$, •OH and $^1O_2$, increasing by 28-, 5.3- and 3.9-fold at pH 6.5, respectively, whereas ZMPF+US only generated the corresponding ROS by 15.2-, 2.7- and 2.1-fold under the same conditions (Figure 3C, F and I). Notably, ZMPF+H_2O_2+US exhibited higher ROS generation at pH 5.5 than at pH 6.5 as acidic conditions favored the chemodynamic process (Figure 3D, G and J). Interestingly, at pH 5.5, the production of $O_2^{\bullet-}$ in the ZMPF+H_2O_2+US group reached up to 54.6-fold, higher than the sum of ZMPF+H_2O_2 (28.5-fold) and ZMPF+US (14.9-fold) (Figure 3D). Moreover, similar results of •OH and $^1O_2$ were observed (Figure 3G and J). Remarkably, the ROS level with US at 1 min already exceeded that of the group without US at 5 min, indicating that US markedly accelerated ROS generation. This acceleration may mainly arise from acoustic cavitation, which enhances local mass transfer and H_2O_2 transport toward the MnO_2-containing surface through cavitation-induced fluid motion and shock waves [52]. In addition, transient local high-temperature and high-pressure regions generated during bubble collapse may further accelerate the reaction kinetics [53]. Thus, these results demonstrated that chemodynamic activity enhanced sonodynamic efficiency, and meanwhile US accelerated chemodynamic process, jointly amplifying ROS production. In contrast to ZMPF, ZPF showed no noticeable enhancement in chemodynamic activity at pH 7.4, 6.5, or 5.5, even in the presence of H_2O_2, because of the absence of MnO_2 in ZPF (Figure S6).

In vitro therapeutic performance

To reveal the anticancer effect, the synergistic sonodynamic and chemodynamic therapeutic performance of ZMPF against 4T1 cells (a murine breast cancer cell line) was systematically evaluated. Specifically, to investigate the sono-chemodynamic therapeutic effect of ZMPF at the cellular level under US irradiation, ZPF and ZMPF were incubated with 4T1 cells over a concentration series (0, 5, 10, 15, 20, 25, 30, 50 μg mL^{-1}) for 24 h, respectively. Subsequently, the cell viability was quantified using the Cell Counting Kit-8 assay. Without US, both ZPF and ZMPF showed low cytotoxicity: cell viability remained above 85% even at 50 μg mL^{-1}, confirming good biocompatibility toward the cells when no external stimulus was applied. ZMPF also showed no apparent cytotoxicity toward normal NIH/3T3 cells, with viability above 85% at concentrations up to 50 μg mL^{-1} (Figure S7). However, upon exposure to US (1.0 MHz, 1.5 W cm^{-2}, 3 min, 40% duty cycle), both ZPF and ZMPF demonstrated concentration-dependent cell toxicity. Notably, at 20 μg mL^{-1}, ZMPF showed a significantly higher cytotoxic effect (IC_{50} = 12.55 μg mL^{-1}) on 4T1 cells compared to ZPF (IC_{50} = 18.27 μg mL^{-1}), with a cell kill rate exceeding 70%, which can be ascribed to the additional CDT of ZMPF (Figure 4A). Typically, nanomaterials enter cells *via* receptor-mediated endocytosis [54]. In order to evaluate the cellular uptake behavior, 4T1 cells were incubated with ZMPF labeled with chlorin e6 (Ce6) for confocal laser scanning microscope (CLSM) or fluorescein isothiocyanate (FITC) for flow cytometry. As shown in Figure 4B, Ce6-labeled ZMPF was clearly observed in cell cytoplasm with intracellular red fluorescence signal reaching saturation at 4 h, corresponding to a cellular uptake efficiency of 34.5%. Furthermore, the therapeutic effect of ZMPF under US irradiation was assessed by live/dead staining. Calcein acetoxymethyl ester (Calcein-AM) labeled viable cells green, whereas propidium iodide (PI) labeled dead cells red. Considering that the H_2O_2 levels in tumor tissue were typically around 50-100 μM, we used 100 μM in the cellular experiments [55-56]. As expected, no cell death was observed in control, ZPF and ZMPF groups. When exogenous H_2O_2 was supplemented in different groups without US irradiation, a distinct red fluorescent signal from ZMPF was observed ascribed to its effective CDT activity. Notably, upon US treatment, the ZMPF+H_2O_2+US group displayed the strongest red signal among all groups, demonstrating markedly enhanced anticancer efficacy *via* the synergistic combination of SDT and CDT (Figure 4C). Based on this, intracellular ROS production during US-activated ZMPF treatment was assessed using 2′,7′-dichlorodihydrofluorescein diacetate (DCFH-DA). Within cells, nonfluorescent DCFH-DA was hydrolyzed by esterases to DCFH, which was retained intracellularly. DCFH was then oxidized by ROS to the green fluorescent product 2′,7′-dichlorofluorescein (DCF).

As expected, compared to other groups, the ZMPF+US group exhibited significant green fluorescence (Figure 4D), particularly with a fluorescence intensity 2.36-fold and 1.5-fold higher than those of ZMPF and ZPF+US groups, respectively (Figure 4E). These results indicated that ROS generation of ZMPF mediated by US was substantially more efficient than that produced by CDT alone, and the solution-phase measurements showed the same trend (Figure 3). Elevated ROS levels can induce apoptosis in cancer cells [57]. Here, Annexin V-FITC/PI staining followed by flow cytometry was used to quantify apoptosis after ZMPF treatment. The apoptotic fraction reached 17.34% in the ZMPF+US

group, the highest among all treatments (Figure 4F). This agreed with the viability and ROS measurements (Figure 4A and D). Apoptosis remained low in the other groups, each of which retained more than 88% viable cell populations. Apoptosis-associated protein expressions in 4T1 cells were further assessed by Western blot. ZMPF+US-treated cells showed the lowest Bcl-2 expression and the highest Bax and cleaved Caspase-3 expression across groups (Figure 4G-H). Overall, these findings indicated that ROS overproduction by US-activated ZMPF induced cellular apoptosis. Additionally, the treatment process was depicted in Figure 4I. Collectively, these results demonstrated that ZMPF exhibited superior anticancer efficacy at the cellular level through the synergistic integration of SDT and CDT.

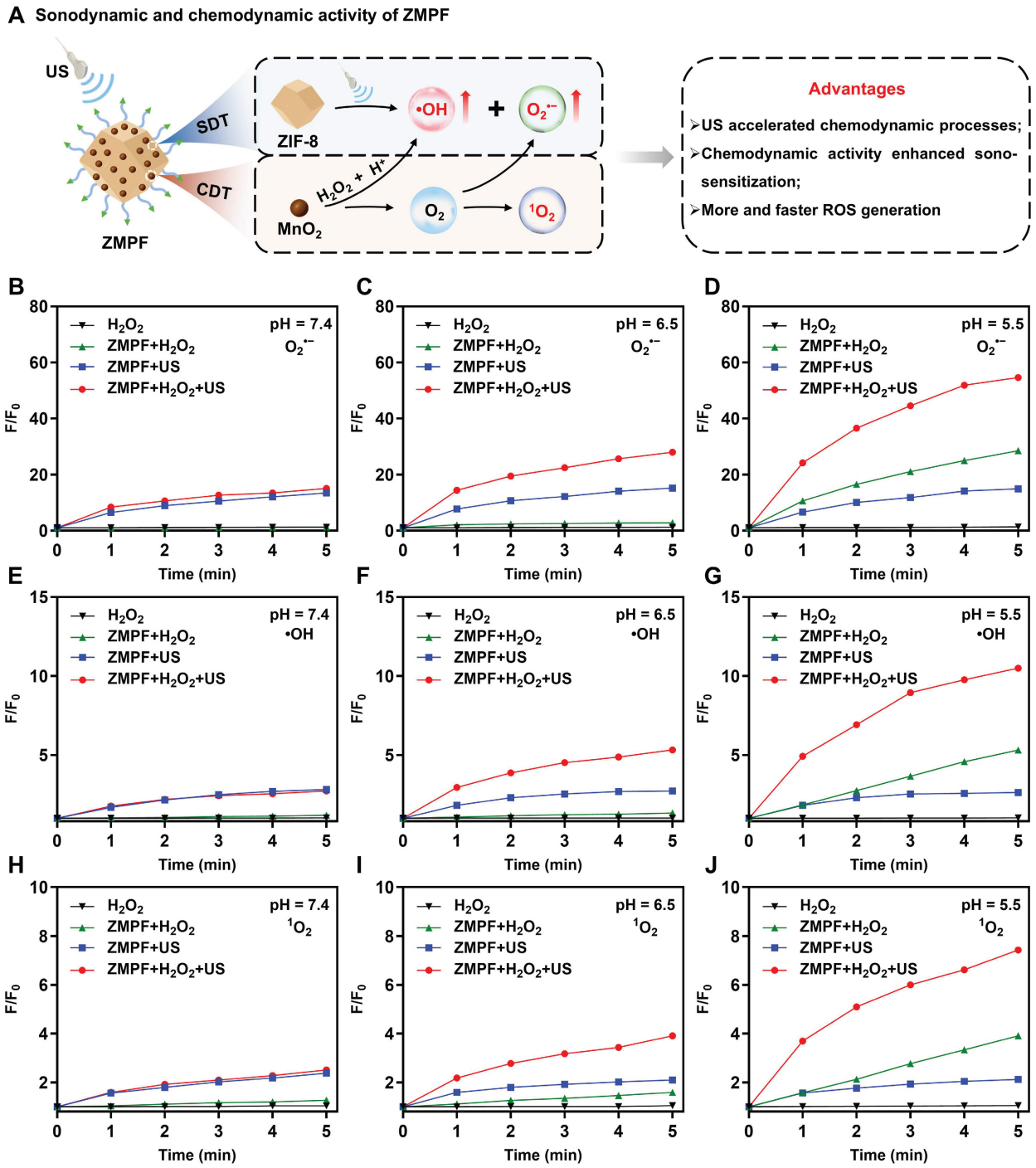


Figure 3. Evaluation of ZMPF-mediated ROS amplification through synergistic sonodynamic and chemodynamic activities. (A) Proposed ROS-generation mechanism involving ZMPF-mediated sonodynamic and chemodynamic activity. ROS generation of $O_2^{\bullet-}$ (B-D), •OH (E-G) and $^1O_2$ (H-J) from H_2O_2, ZMPF+H_2O_2, ZMPF+US and ZMPF+H_2O_2+US groups in 10 mM PBS at pH 7.4, 6.5 or 5.5 (37 ℃), respectively. F/F_0 represented the fluorescence intensity ratio of DHR123, HPF, SOSG before and after the US treatment (1.5 W cm^{-2}, 40% duty cycle) as a function of different treatment times, respectively.

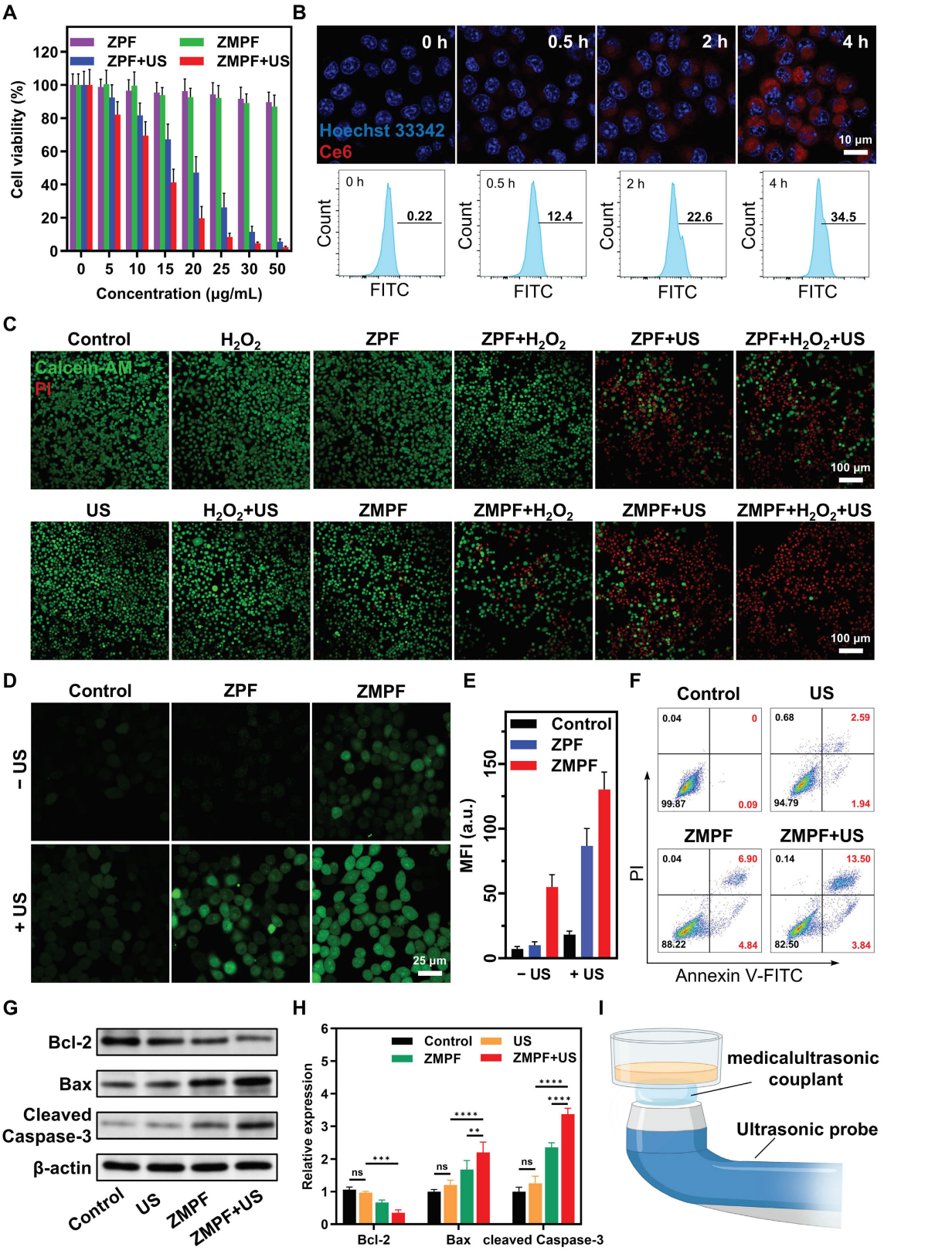


Figure 4. *In vitro* antitumor effect of ZMPF under US irradiation. (A) Viability of 4T1 cells incubated with different concentrations of ZPF or ZMPF in the absence or presence of US treatment (1.0 MHz, 1.5 W cm^{-2}, 40% duty cycle, 3 min), respectively. Data were shown as mean ± s.d. (n = 6). (B) Confocal fluorescent images and flow-cytometry quantification of 4T1 cell uptake after incubation with ZMPF@Ce6 (confocal) or ZMPF@FITC (flow cytometry) at different timepoints (0, 0.5, 2 and 4 h), respectively. Nuclei were stained with Hoechst 33342 (blue). (C) Confocal images of 4T1 cells co-stained with Calcein-AM and PI after the indicated treatments. (D) Confocal images of intracellular ROS in 4T1 cells incubated with ZPF or ZMPF in the presence or absence of US treatment. Green signal of the oxidative state of DCFH-DA (10 μM) was observed after 20 min incubation. (E) Quantification of green signal in Figure 4D. Data were presented as mean ± s.d. (n = 3). (F) Flow-cytometric apoptosis analysis of control, US, ZMPF and ZMPF+US groups. (G) Western blot analysis of expression levels of apoptosis-related proteins (Bcl-2, Bax and cleaved Caspase-3) in 4T1 cells following various treatments. (H) The corresponding quantitative analysis of Figure 4G. Two-way ANOVA. ns: $p > 0.05$, ***$p < 0.001$, ****$p < 0.0001$ (n = 3, mean ± s.d.). (I) Schematic illustration of the experimental step for US treatment of cells.

RNA sequencing transcriptome analysis

To gain deeper insight into the antitumor mechanisms of ZMPF-mediated SDT/CDT combination therapy *in vitro*, the transcriptome of treated 4T1 cells was profiled by RNA sequencing to analyze the gene expression. Principal component analysis (PCA) showed that replicates within each group clustered closely, while clear separation was observed between groups (Figure 5A). Compared with control group, ZMPF+US group displayed a total of 4156 differentially expressed genes (DEGs, Padjust < 0.05 and fold change ≥ 2), including 2428 upregulated genes and 1728 downregulated genes (Figure 5B). ZMPF+US treatment upregulated Tnfsf13b (encoding B-cell activating factor, BAFF) and tumor-suppressor genes, while downregulating genes associated with tumor growth (Pik3c3) and metastasis (Fgf2, Enpp4, Mmp28, Mmp15, and Mmp11). These expression changes were consistent with the clustering patterns shown in the heatmap (Figure S8), indicating that ZMPF+US inhibited proliferation and migration [58-61]. Pathway enrichment analyses were then carried out to identify the cellular processes most affected by ZMPF+US treatment in 4T1 cells. Gene ontology (GO) analysis indicated that the DEGs were enriched in apoptotic process, cellular redox homeostasis, DNA damage response and cell proliferation (Figure 5C), all of which were closely associated with tumor development and therapeutic response. The relative enrichment levels of these GO terms were summarized in a circular plot (Figure 5D). Kyoto encyclopedia of genes and genomes (KEGG) analysis revealed enrichment in cancer-related pathways, including the MAPK, p53 and PI3K-Akt pathways, helping to explain the strong tumor suppression observed in the ZMPF+US group (Figure 5E). The links between individual DEGs and these key KEGG pathways were visualized in a chord diagram (Figure 5F). Furthermore, heat maps were generated to analyze the specific antitumor genes above DEGs. Numerous apoptosis-related genes, such as Bcl2l11, Cycs, Gadd45g, Gadd45b, Gadd45a, Ddit3, Atf4 and Mapk8, were markedly upregulated in ZMPF+US group. Meanwhile, genes involved in oxidative stress responses (Cyp1a1 and Cyp1b1) and GSH metabolism (Gclc, Gclm and Chac1) were also significantly modulated, indicating massive ROS generation induced by SDT and CDT. Moreover, in the ZMPF+US group, genes associated with signaling and stress as well as growth regulation were profoundly altered, as reflected by the downregulation of related genes (signaling and stress: Pdgfra, Pdgfrb, Erbb2 and Ibsp; growth regulation: Tgfb3, Acvr1b, Lrrc32 and Rgma) and the upregulation of the cell-cycle-arrest gene (Cdkn1a) (Figure 5G). Subsequently, the protein-protein interaction (PPI) network was constructed to map the functional relationships between the proteins encoded by these DEGs. At the level of protein cooperation, the network reinforced the link between apoptosis regulators (*e.g.*, Gadd45b, Atf4) and oxidative-stress mediators (*e.g.*, Gsta1, Cyp1b1), thereby connecting transcriptomic changes to a coherent functional regulatory network (Figure S9). Finally, gene set enrichment analysis (GSEA) was applied at the systems level to better characterize the gene-expression shifts driven by ZMPF+US in 4T1 cells. The analysis identified strong enrichment of oncogenic gene sets such as hallmark apoptosis and hallmark P53 pathway in the ZMPF+US group (Figure 5H), consistent with the KEGG findings and providing additional support that cellular apoptosis was successfully induced in 4T1 cells. Additional metalloimmunological analysis indicated activation of cGAS-STING signaling following ZMPF+US treatment (**Figure S10**), consistent with previous reports that Mn^{2+} and Zn^{2+} can enhance cGAS-STING signaling [62-64]. To assess differences between the combined treatment and either single modality, additional transcriptomic analyses of ZMPF+US vs. ZMPF and ZMPF+US vs. ZPF+US were performed. In both comparisons, DEGs were enriched in apoptosis, MAPK, p53, and cytosolic DNA-sensing pathways (**Figure S11A, B**). Consistent expression changes were observed in genes associated with apoptosis, MAPK signaling, p53 signaling, and DNA-sensing/IFN responses (**Figure S11C,D**). These transcriptional differences were therefore observed not only relative to untreated cells but also relative to both single-modality controls. Taking together, the transcriptomic data indicated that US-activated ZMPF suppressed 4T1 cells mainly through ROS-associated apoptosis, while metal-ion-mediated immune regulation may also contribute to this effect.

In vivo real-time MRI of tumor

Before animal studies, the hemolysis and complete blood count analysis of ZMPF were systematically evaluated (Figure S12-13). ZMPF induced no detectable hemolysis even at 25 μg mL^{-1} and exhibited good systemic tolerance at a high dosage of 10 mg kg^{-1}, demonstrating the excellent biocompatibility. To further investigate the *in vivo* diagnostic and therapeutic performance of ZMPF, MRI and SDT were longitudinally conducted in 4T1 tumor-bearing mice. ZPF and ZMPF were intravenously administered to the 4T1 tumor-bearing mice seven days after tumor implantation, respectively, followed by real-time MRI monitoring (Figure 6A).

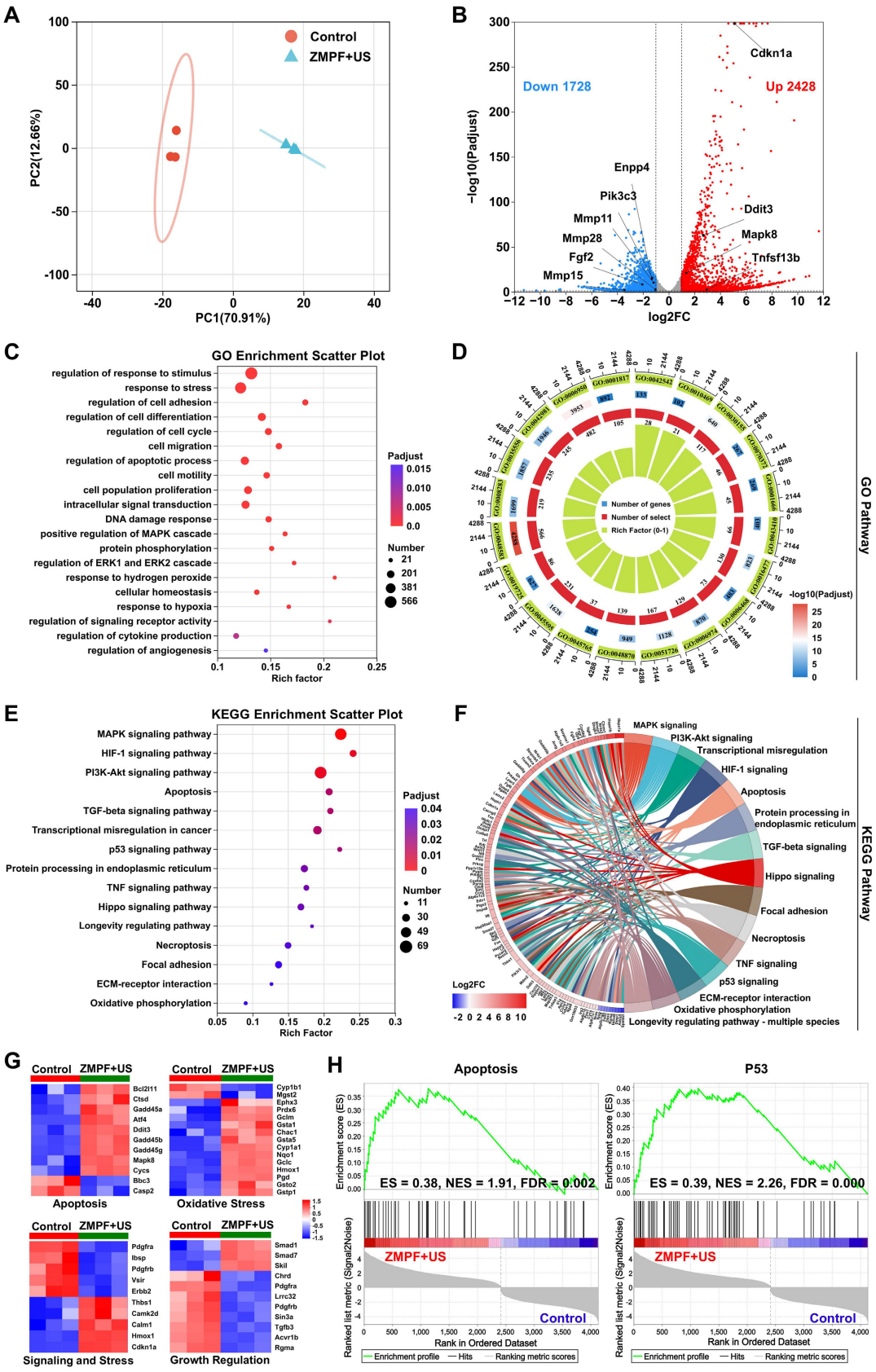


Figure 5. RNA sequencing analysis of 4T1 cells (control group vs. ZMPF+US-treated group). (A) PCA of the samples from ZMPF+US group and control group. ZMPF+US group: 4T1 cells treated with ZMPF NPs upon US irradiation, control group: cells without any treatment. (B) Volcano plot of DEGs between control and ZMPF+US group, with genes meeting Padjust of < 0.05 and fold change ≥ 2 highlighted in blue (down-regulated) and red (up-regulated). (C) GO enrichment of RNA-seq DEGs after ZMPF+US treatment. (D) Circular diagram between DEGs and GO pathways. (E) Bubble diagram of the DEGs enriched in the KEGG pathway. (F) Chord diagram data of KEGG enrichment analysis of apoptosis-related DEGs. (G) Heatmaps of DEGs associated with apoptosis, oxidative stress, signaling and stress, and growth regulation. (H) GSEA enrichment plots of hallmark apoptosis and hallmark P53 pathway gene sets in the ZMPF+US treated as compared to the nontreated control.

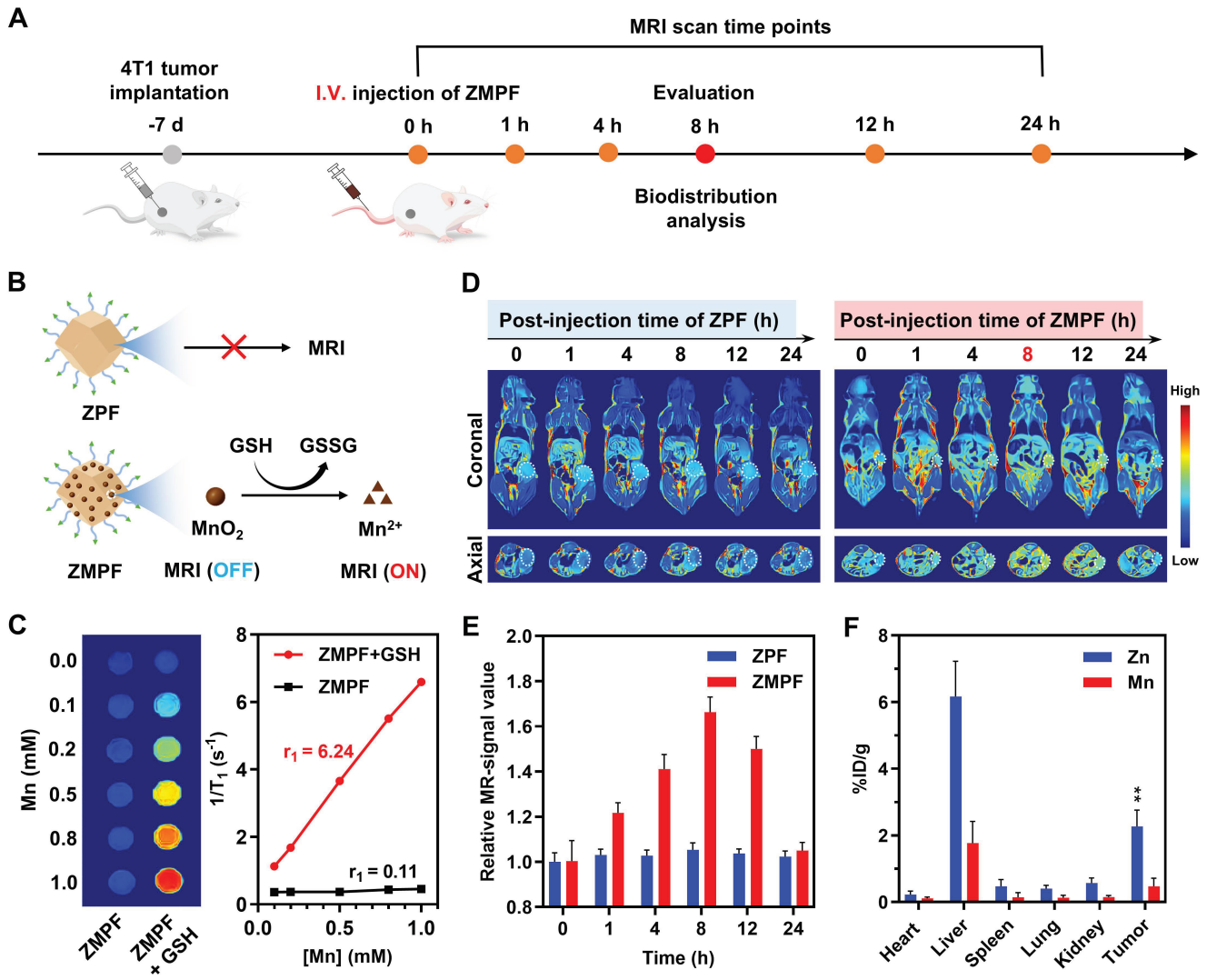


Figure 6. T_1-weighted MR imaging and biodistribution of ZMPF in 4T1 tumor-bearing mice. (A) Timeline of the MR imaging schedule. (B) Schematic illustration of MR signal change of ZPF and ZMPF against GSH, respectively. (C) *In vitro* T_1-weighted MR images and the longitudinal relaxivity (r_1) of ZMPF with and without GSH. (D) *In vivo* real-time T_1-weighted MRI of 4T1 tumor-bearing mice before and after intravenous injection of ZPF and ZMPF at different time points, respectively. The white circles indicated the tumor region. The upper and lower rows showed coronal and axial views, respectively. (E) Quantification of T_1-MR signals from tumor in 6D (n = 3, mean ± s.d.). (F) ICP-based biodistribution study of Zn and Mn ions from major organs of 4T1 tumor-bearing mice at 8 h post-intravenous injection of ZMPF (n = 3, mean ± s.d.). Statistical analysis in F was performed using one-way ANOVA. **p < 0.01 for Zn accumulation in tumors versus that in the heart, spleen, lung and kidney.

First, the tumor microenvironment (TME) mechanism of ZMPF was examined. ZMPF was efficiently decomposed with GSH to release Mn^{2+} ions, which served as an MRI contrast agent for tumor specific imaging, whereas no discernible MRI signal was detectable for ZPF (Figure 6B) [65-66]. Moreover, the content of Mn element in ZMPF was determined to be 92.174 mg L^{-1} by inductively coupled plasma-optical emission spectrometry (ICP-OES, Table S1). Notably, ZMPF showed a markedly enhanced longitudinal relaxivity (r_1) of 6.24 mM^{-1} s^{-1} following GSH treatment, significantly higher than that observed in the absence of GSH (Figure 6C). Subsequently, the real-time MRI of ZPF and ZMPF was conducted at different post-injection times (0, 1, 4, 8, 12 and 24 h) using a 0.5 T MR scanner. After ZMPF administration, the T_1-weighted MR signal in the tumor region gradually increased owing to active tumor targeting. It reached a plateau at 8 h and was approximately 1.66-fold higher than that in the MnO_2-free ZPF group (Figure 6D-E and Figure S14). In addition, compared with FA-free ZMP (ZIF-8@MnO_2-PEG), ZMPF showed a higher peak tumor MR signal and reached it earlier (8 versus 12 h; Figure S15). This result supported FA-mediated active tumor targeting. Furthermore, the *in vivo* biodistribution of Zn and Mn was quantified by ICP analysis at 8 h after intravenous injection of ZMPF (Figure 6F). Both Zn and Mn accumulated mainly in the liver and tumor. The Zn levels in these two tissues were 6.17 and 2.26 %ID/g, respectively. The higher liver uptake was consistent with hepatic sequestration by the reticuloendothelial

system, which contributed to nanoparticle clearance from circulation. These results suggested that FA-mediated tumor accumulation coexisted with substantial hepatic uptake. Taken together, these results confirmed that ZMPF can serve as a TME-responsive T_1-weighted MRI contrast agent *in vivo*.

In vivo sono-chemodynamic therapeutic performance

Motivated by the promising therapeutic effects observed *in vitro* and MRI guidance, anti-cancer effects *in vivo* were investigated using 4T1 subcutaneous model in 5-week-old female BALB/c mice. First, the tumor-bearing mice were randomly divided into six groups (control, US, ZPF, ZMPF, ZPF+US, and ZMPF+US). An intravenous dose of 10 mg kg^{-1} of ZPF or ZMPF was administered on days 0, 2 and 4, respectively, and the tumors were exposed to US 8 h after intravenous injection (US parameters: 1.0 MHz, 1.5 W cm^{-2}, 40% duty cycle, 5 min). Body weight and tumor volume were measured in each group every two days. All mice were humanely sacrificed on day 14. Organs and tumors were collected for further analysis (Figure 7A). Over the 14-day treatment period, the body weight increased modestly in all groups with no significant inter-group differences, indicating the safety of ZMPF-mediated sono-chemodynamic treatment (Figure 7B). Tumor volume analysis revealed that the tumor inhibition rates in ZPF+US and ZMPF+US groups reached up to 84.6% and 99.2%, respectively, whereas ZPF and ZMPF groups only showed slight inhibition of tumor growth (Figure 7C). The photograph of excised tumors clearly manifested the decreased tumor size among the mice in the ZMPF+US group in comparison to the other groups, thus emphasizing the remarkable anti-tumor effect (Figure 7D). The individual tumor volume curves further confirmed the above results (Figure 7E). Consistent with previous findings, these results demonstrated that ZMPF can mediate US to enhance the sono-chemodynamic effect for the treatment of *in vivo* tumors.

Moreover, hematoxylin & eosin (H&E) staining of major organs (heart, liver, spleen, lung and kidney) revealed no obvious histopathological damage or inflammation, further indicating favorable biosafety of ZMPF *in vivo* (Figure S16). Finally, the antitumor mechanism within the tumor was evaluated by histological analyses of tumor tissue, including H&E, terminal deoxynucleotidyl transferase dUTP nick-end labeling (TUNEL) and dihydrorhodamine 123 (DHR123) fluorescence staining (Figure 7F). The H&E staining showed the most severe cellular necrosis and damage in the ZMPF+US group. The TUNEL staining assay uncovered a substantial number of fragmented DNAs, indicating a more pronounced apoptosis signal intensity within the tumor cells shown in the ZMPF+US group. Intratumoral ROS levels were assessed using DHR123 as the fluorescent probe. The strongest green fluorescence was detected in the ZMPF+US group, confirming robust ROS generation *in vivo*. Semi-quantitative analysis of the TUNEL and DHR123 staining agreed with the histological observations (Figure S17). Overall, these results verified that ZMPF+US had the potential to serve as a highly effective ROS-based treatment strategy of solid tumors, thereby reinforcing the conclusion that apoptosis played a central role in the mechanism of the therapeutic strategy.

Conclusions

In conclusion, we developed a TME-activatable ZMPF nanoplatform for MRI-guided sono-chemodynamic tumor therapy by integrating a ZIF-8 sonosensitizer framework, MnO_2 catalytic decoration, and FA-mediated targeting. Beyond establishing an integrated sono-chemodynamic therapeutic system, this work provides the first systematic elucidation of the bidirectional kinetic interplay between SDT and CDT. For SDT, upon US treatment, ZMPF preferentially generated $O_2^{\bullet-}$ through ZIF-8-mediated SDT, with a 14.1-fold enhancement over other ROS species. Specifically, for synergistic SDT and CDT, US-treated ZMPF displayed 54.6-fold enhancement for $O_2^{\bullet-}$ generation under acidic H_2O_2 conditions. This value exceeded those of SDT alone (14.9-fold) and CDT alone (28.5-fold), demonstrating synergy beyond simple additivity. At the cellular level, ZMPF+US caused robust ROS accumulation and apoptosis, affording a low IC_{50} of 12.55 μg mL^{-1} in 4T1 cells. RNA sequencing further revealed that this treatment reprogrammed oxidative stress, apoptotic signaling, and growth regulation in 4T1 cells, providing molecular evidence for sono-chemodynamic therapy. In addition, GSH-triggered MnO_2-based ZMPF with robust T_1-weighted MRI contrast (r_1 = 6.24 mM^{-1} s^{-1}) and a 1.66-fold tumor signal increase was further utilized for effective tracking of tumor accumulation *in vivo*. Subsequent US irradiation achieved a remarkable tumor inhibition rate of 99.2% with excellent biosafety. Overall, this study not only establishes ZMPF as a mechanistically informed platform for MRI-guided precision sono-chemodynamic therapy but also provides a design paradigm for bidirectionally amplified SDT/CDT nanomedicine. In the future, we will further investigate the immunomodulatory mechanism of ZMPF-mediated sono-chemodynamic therapy.

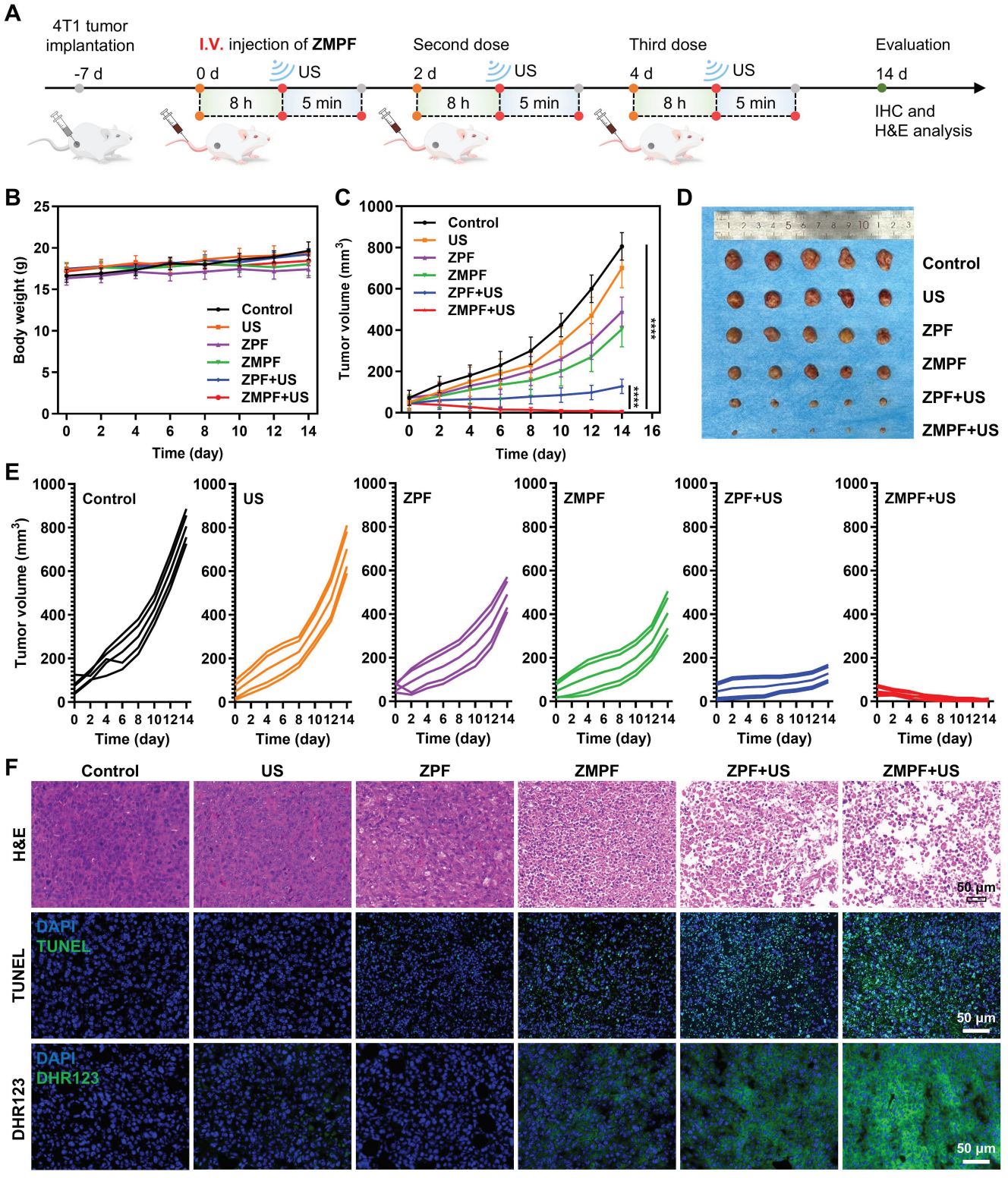


Figure 7. *In vivo* antitumor performance of ZMPF under US irradiation. (A) Timeline of the therapeutic schedule. IHC means immunohistochemistry. (B) Body weight of 4T1 tumor-bearing mice after indicated treatments (n = 5 mice, mean ± s.d.). (C) Tumor-volume curves of 4T1 tumor-bearing mice after indicated treatments. (ZMPF+US vs. Control and ZMPF+US vs. ZPF+US at day 14: two-tailed unpaired Student's t-test, ****$p < 0.0001$; n = 5 mice, mean ± s.d.). (D) Photographs of tumors excised from each group on day 14 of different treatments. (E) Individual tumor growth curves of mice after different treatments. (F) Representative H&E, TUNEL and DHR123 staining images of tumor tissues after indicated treatments (n = 3 independent experiments). Nuclei were stained with DAPI (blue), apoptotic DNA fragments were stained with TUNEL (green) and $O_2^{\cdot-}$ were stained with DHR123 (green). Scale bar = 50 μm.

Abbreviations

SDT: sonodynamic therapy; CDT: chemodynamic therapy; TME: tumor microenvironment; MRI: magnetic resonance imaging; US: ultrasound; ROS: reactive oxygen species; PEG-FA: polyethylene glycol-folic acid; GSH: glutathione; TEM: transmission electron microscopy; EDX: energy dispersive X-ray; XPS: X-ray photoelectron spectroscopy; XRD: X-ray diffraction; FT-IR: Fourier transform infrared; DI water: deionized water; DHR123: dihydrorhodamine 123; CLSM: confocal laser scanning microscope; Ce6: chlorin e6; FITC: fluorescein isothiocyanate; PI: propidium iodide; DCFH-DA: 2′,7′-dichlorodihydrofluorescein diacetate; DEGs: differentially expressed genes; GO: Gene Ontology; KEGG: Kyoto Encyclopedia of Genes and Genomes; PPI: protein-protein interaction; GSEA: gene set enrichment analysis; ICP-OES: inductively coupled plasma-optical emission spectrometry; H&E: hematoxylin & eosin; TUNEL: terminal deoxynucleotidyl transferase dUTP nick-end labeling.

Supplementary Material

Supplementary methods, figures and tables.
https://www.thno.org/v17p0589s1.pdf

Acknowledgments

This research was funded by the National Natural Science Foundation of China, grant numbers 12374445 and 82061148015. Certain graphical elements in Scheme 1, Figure 6, Figure 7, and TOC were created using BioRender.com. L. S. acknowledges support from China Scholarship Council (grant 202506280144).

Author contributions

L.S. conceived the experimental protocol, conducted the experiments and drafted the manuscript. C.H. and Z.N. contributed to investigation. Y.L., J.L., and M.W. assisted in review. P.L. supervised the work and reviewed the manuscript. Y.F. contributed to conceptualization, funding acquisition, supervision, and manuscript editing. All authors participated in discussing the results and reviewing the manuscript.

Ethics approval and consent to participate

All animal experiments reported were performed under the guidelines of the Committee of Animal Experimentation and the Ethics Committee, Xi'an Jiaotong University (XJTUBME-202657).

Data availability

Data will be made available on request.

Competing Interests

The authors have declared that no competing interest exists.

References

1. Mitragotri S. Healing sound: The use of ultrasound in drug delivery and other therapeutic applications. Nat Rev Drug Discov. 2005; 4: 255-260.
2. Qian X, Zheng Y, Chen Y. Micro/nanoparticle-augmented sonodynamic therapy (SDT): breaking the depth shallow of photoactivation. Adv Mater. 2016; 28: 8097-8129.
3. Helmlinger G, Yuan F, Dellian M, Jain RK. Interstitial pH and pO_2 gradients in solid tumors in vivo: high-resolution measurements reveal a lack of correlation. Nat Med. 1997; 3: 177-182.
4. Singleton DC, Macann A, Wilson WR. Therapeutic targeting of the hypoxic tumour microenvironment. Nat Rev Clin Oncol. 2021; 18: 751-772.
5. Wen D, Feng J, Deng R, Li K, Zhang H. Zn/Pt dual-site single-atom driven difunctional superimposition-augmented sonosensitizer for sonodynamic therapy boosted ferroptosis of cancer. Nat Commun. 2024; 15: 9359.
6. Fu LH, Qi C, Hu YR, Lin J, Huang P. Glucose oxidase-instructed multimodal synergistic cancer therapy. Adv Mater. 2019; 31: 1808325.
7. Sun L, Zhou JE, Luo T, Wang J, Kang L, Wang Y, et al. Nanoengineered neutrophils as a cellular sonosensitizer for visual sonodynamic therapy of malignant tumors. Adv Mater. 2022; 34: 2109969.
8. Pan Y, Liu L, Mou X, Cai Y. Nanomedicine strategies in conquering and utilizing the cancer hypoxia environment. ACS Nano. 2023; 17: 20875-20924.
9. Zhang M, Sun D, Huang H, Yang D, Song X, Feng W, et al. Nanosonosensitizer optimization for enhanced sonodynamic disease treatment. Adv Mater. 2024; 36: 2409663.
10. Ding Q, Li W, Mei L, Luo S, Tao J, Shi C, et al. Tailoring advanced metal-based nanomedicines for adaptable nanodynamic disease therapies and theranostics. Adv Mater. 2026; 38: e13609.
11. Liu Z, Li F, Sun J, Li Z, Li K, Zheng M, et al. Reversible metal coordination switch enables activatable sonodynamic therapy via dual-death and immune synergy. Adv Mater. 2026; 38: e21565.
12. Xu Z, Zeng Y, Kang M, Zhang Z, Yang Z, Fan M, et al. Dual-enhanced sonodynamic therapy: synergizing cavitation amplification and efficient sonoluminescence-to-ROS conversion for orthotopic breast cancer treatment. Adv Mater. 2026; 38: e16803.
13. Wang W, Pan X, Yang H, Wang H, Wu Q, Zheng L, et al. Bioactive metal-organic frameworks with specific metal-nitrogen (M-N) active sites for efficient sonodynamic tumor therapy. ACS Nano. 2021; 15: 20003-20012.
14. Pan X, Huang Z, Guo J, Wu Q, Wang C, Zhang H, et al. MOF-derived nanoparticles with enhanced acoustical performance for efficient mechano-sonodynamic therapy. Adv Mater. 2024; 36: 2400142.
15. Zhu P, Chen Y, Shi J. Nanoenzyme-augmented cancer sonodynamic therapy by catalytic tumor oxygenation. ACS Nano. 2018; 12: 3780-3795.
16. Huang P, Qian X, Chen Y, Yu L, Lin H, Wang L, et al. Metalloporphyrin-encapsulated biodegradable nanosystems for highly efficient magnetic resonance imaging-guided sonodynamic cancer therapy. J Am Chem Soc. 2017; 139: 1275-1284.
17. Liao M, Zhang Q, Huang J, Huang X, Cheng C, Tu J, et al. Near-infrared and ultrasound triggered Pt/Pd-engineered cluster bombs for the treatment of solid tumors. J Control Release. 2024; 375: 331-345.
18. Zhu K, Wang J, Wang Z, Chen Q, Song J, Chen X. Ultrasound-activated theranostic materials and their bioapplications. Angew Chem Int Ed Engl. 2025; 64: e202422278.
19. Xiao L, Cai J, Wang Y, Hu J, Dou H, Pan D, et al. Zr-based metal-organic framework dual-sensitized by carbon dot sonosensitizers and MnO_{2-x} nanozymes for cGAS-STING activation enhanced sonocatalytic-immunotherapy. Adv Funct Mater. 2026; 36: e19998.
20. Hu J, Xiang Y, Zhang Z, Cai J, Wang Y, Dou H, et al. Atomic-valence engineering of a Mn (III)-tuned sonozyme system for multimodal tumor immunotherapy. Biomaterials. 2026; 329: 123987.
21. Pan M, Hu D, Yuan L, Yu Y, Li Y, Qian Z. Newly developed gas-assisted sonodynamic therapy in cancer treatment. Acta Pharm Sin B. 2023; 13: 2926-2954.
22. Cai L, Du J, Han F, Shi T, Zhang H, Lu Y, et al. Piezoelectric metal-organic frameworks based sonosensitizer for enhanced nanozyme catalytic and sonodynamic therapies. ACS Nano. 2023; 17: 7901-7910.
23. Li F, Li T, Li K, Meng M, Guo X, He S, et al. Organic semiconducting sono-metallo-detonated immunobombs for ultrasensitized domestication of immunosuppressive cells. Nano Lett. 2024; 24: 7340-7349.
24. Lu Z, Bai S, Jiang Y, Wu S, Xu D, Zhang J, et al. Amplifying dendritic cell activation by bioinspired nanometal organic frameworks for synergistic sonoimmunotherapy. Small. 2022; 18: 2203952.
25. Wang D, Ji L, Li Y, Xu M, Wang H, Brovelli S, et al. Iron-silver-modified quantum dots act as efficient catalysts in anti-cancer multitherapy through controlled, ultrasound-induced oxidation. Nat Nanotechnol. 2025; 20: 1098-1107.

26. Tong Y, Li M, Huang H, Long S, Sun W, Du J, et al. Urea-bond scission induced by therapeutic ultrasound for biofunctional molecule release. J Am Chem Soc. 2022; 144: 16799-16807.
27. Liu S, Li J, Wang A, Ng DKP, Zheng N. Multicomponent polymerization toward poly(BODIPY-sulfonamide)s as unique SO_2 generators for sonodynamic and gas combination therapy. Angew Chem Int Ed Engl. 2025; 64: e202422362.
28. Zhang C, Huang J, Zeng Z, He S, Cheng P, Li J, et al. Catalytical nano-immunocomplexes for remote-controlled sono-metabolic checkpoint trimodal cancer therapy. Nat Commun. 2022; 13: 3468.
29. Liu S, Meng Q, Liu Z, Wang J, Li J, Ma X, et al. Engineered metal-organic framework with stereotactic anchoring and spatial separation of porphyrins for amplified ultrasound-mediated pyroptosis and cancer immunotherapy. Angew Chem Int Ed Engl. 2025; 64: e202421402.
30. Wang C, Fan W, Zhang Z, Wen Y, Xiong L, Chen X. Advanced nanotechnology leading the way to multimodal imaging-guided precision surgical therapy. Adv Mater. 2019; 31: 1904329.
31. Wu Q, Yao X, Duan X, Chen X, Zhang J. Nanomedicine reimagined: translational strategies for precision tumor theranostics. Adv Mater. 2026; 38: e10293.
32. Mieog JSD, Achterberg FB, Zlitni A, Hutteman M, Burggraaf J, Swijnenburg RJ, et al. Fundamentals and developments in fluorescence-guided cancer surgery. Nat Rev Clin Oncol. 2022; 19: 9-22.
33. Li J, Pu K. Development of organic semiconducting materials for deep-tissue optical imaging, phototherapy and photoactivation. Chem Soc Rev. 2019; 48: 38-71.
34. Li B, Zhao M, Lin J, Huang P, Chen X. Management of fluorescent organic/inorganic nanohybrids for biomedical applications in the NIR-II region. Chem Soc Rev. 2022; 51: 7692-7714.
35. Hou X, Ren C, Zeng X, Hu Y, Zhao Y, Cheng Y, et al. Co-delivery of SN38 and SR717 activates cGAS-STING for near-infrared II image-guided chemoimmunotherapy. J Control Release. 2025; 386: 114129.
36. Ou Z, Duh YS, Rommelfanger NJ, Keck CH, Jiang S, Brinson Jr K, et al. Achieving optical transparency in live animals with absorbing molecules. Science. 2024; 385: eadm6869.
37. Luo L, Wu M, Li M, Xin Y, Wang Q, Vardhanabhuti V, et al. A large model for non-invasive and personalized management of breast cancer from multiparametric MRI. Nat Commun. 2025; 16: 3647.
38. Sack I. Magnetic resonance elastography from fundamental soft-tissue mechanics to diagnostic imaging. Nat Rev Phys. 2023; 5: 25-42.
39. Lu C, Liao S, Chen B, Xu L, Wu N, Lu D, et al. Responsive probes for in vivo magnetic resonance imaging of nitric oxide. Nat Mater. 2025; 24: 133-142.
40. Mi P, Kokuryo D, Cabral H, Wu H, Terada Y, Saga T, et al. A pH-activatable nanoparticle with signal-amplification capabilities for non-invasive imaging of tumour malignancy. Nat Nanotechnol. 2016; 11: 724-730.
41. Choi JS, Kim S, Yoo D, Shin TH, Kim H, Gomes MD, et al. Distance-dependent magnetic resonance tuning as a versatile MRI sensing platform for biological targets. Nat Mater. 2017; 16: 537-542.
42. Lu Y, Xu YJ, Zhang GB, Ling D, Wang MQ, Zhou Y, et al. Iron oxide nanoclusters for T_1 magnetic resonance imaging of non-human primates. Nat Biomed Eng. 2017; 1: 637-643.
43. Shi C, Zhang Q, Yao Y, Zeng F, Du C, Nijiati S, et al. Targeting the activity of T Cells by membrane surface redox regulation for cancer theranostics. Nat Nanotechnol. 2023; 18: 86-97.
44. Zhang C, Nan B, Xu J, Yang T, Xu L, Lu C, et al. Magnetic-susceptibility-dependent ratiometric probes for enhancing quantitative MRI. Nat Biomed Eng. 2025; 9: 671-685.
45. Huo L, Zeng J, Wang Z, Sun X, Guo Y, Cao Z, et al. Magnetic field-optimized paramagnetic nanoprobe for T_2/T_1 switchable histopathological-level MRI. ACS Nano. 2024; 18: 12453-12467.
46. Lu H, Chen A, Zhang X, Wei Z, Cao R, Zhu Y, et al. A pH-responsive T_1-T_2 dual-modal MRI contrast agent for cancer imaging. Nat Commun. 2022; 13: 7948.
47. Liu Y, Gong CS, Dai Y, Yang Z, Yu G, Liu Y, et al. In situ polymerization on nanoscale metal-organic frameworks for enhanced physiological stability and stimulus-responsive intracellular drug delivery. Biomaterials. 2019; 218: 119365.
48. Wang H, Pei X, Kalmutzki MJ, Yang J, Yaghi OM. Large cages of zeolitic imidazolate frameworks. Acc Chem Res. 2022; 55: 707-721.
49. Jin W, Bor G, Asgari M, Bochsen L, Qvortrup K, Krogh AKH, et al. Biorthogonal PEGylation of hierarchical porous metal-organic frameworks as robust, functional nanocarriers for hemoglobin-based oxygen delivery. J Am Chem Soc. 2025; 147: 43400-43414.
50. Liu X, Wang J, Wu Y, Wu M, Song J. Ultrasound activated probe for disease imaging and therapy in-vivo. Adv Drug Deliv Rev. 2024; 205: 115158.
51. Li B, Ye X, Fu Y, Feng L, Xu J, Niu X, et al. Hollow MnO_2-based nanoprobes for enhanced photothermal/photodynamic/chemodynamic co-therapy of hepatocellular carcinoma. Pharm Res. 2023; 40: 1271-1282.
52. Pan Y, Li R, Zhang L, Liu JX, Wang W, Zhang GJ. Catalyst-free partial oxidation of methane under ambient conditions boosted by mechanical stirring-enhanced ultrasonic cavitation. Nat Commun. 2025; 16: 7506.
53. Mahendran V, Trinh QT, Zhangyue X, Jonnalagadda U, Gould T, Nguyen NT, et al. Localized oxidative catalytic reactions triggered by cavitation bubbles confinement on copper oxide microstructured particles. Angew Chem Int Ed Engl. 2025; 64: e202416543.
54. Banushi B, Joseph SR, Lum B, Lee JJ, Simpson F. Endocytosis in cancer and cancer therapy. Nat Rev Cancer. 2023; 23: 450-473.
55. Wang X, Fu J, Jiang C, Liao X, Chen Y, Jia T, et al. Specific and long-term luminescent monitoring of hydrogen peroxide in tumor metastasis. Adv Mater. 2023; 35: 2210948.
56. Bai L, Yang J, Yu S, Xiang Z, Zeng Y, Shen M, et al. Self-sufficient nanoparticles with dual-enzyme activity trigger radical storms and activate cascade-amplified antitumor immunologic responses. Acta Pharm Sin B. 2024; 14: 821-835.
57. Wu S, Xia X, Zhou R, Zhao H. Hydrogel-enabled ROS-GSH modulation for sustained copper-mediated chemodynamic therapy of oral squamous cell carcinoma. J Control Release. 2025; 383: 113772.
58. Hao X, Shen Y, Liu J, Alexander A, Wu L, Xu Z, et al. Solid tumour-induced systemic immunosuppression involves dichotomous myeloid-B cell interactions. Nat Cell Biol. 2024; 26: 1971-1983.
59. Swamynathan MM, Kuang S, Watrud KE, Doherty MR, Gineste C, Mathew G, et al. Dietary pro-oxidant therapy by a vitamin K precursor targets PI 3-kinase VPS34 function. Science. 2024; 386: eadk9167.
60. Elkholi IE, Robert A, Malouf C, Wu JL, Kuasne H, Drapela S, et al. Targeting the dependence on PIK3C3-mTORC1 signaling in dormancy-prone breast cancer cells blunts metastasis initiation. Cancer Res. 2025; 85: 2179-2198.
61. Zhang C, Yuan L, Wen W, Shao C, Liao Y, Jia Y, et al. LNMAC promotes cervical squamous cell carcinoma lymphatic metastasis via epigenetic regulation of FGF2-induced lymphangiogenesis. Adv Sci. 2024; 11: 2404645.
62. Yang N, Sun S, Xu J, Gong F, Lei H, Hao Y, et al. Manganese galvanic cells intervene in tumor metabolism to reinforce cGAS-STING activation for bidirectional synergistic hydrogen-immunotherapy. Adv Mater. 2025; 37: 2414929.
63. Song J, Wang H, Meng X, Li W, Qi J. A hypoxia-activated and microenvironment-remodeling nanoplatform for multifunctional imaging and potentiated immunotherapy of cancer. Nat Commun. 2024; 15: 10395.
64. Yang L, Wang Y, Song Y, Li Z, Lei L, Li H, et al. Metal coordination nanotheranostics mediated by nucleoside metabolic inhibitors potentiate STING pathway activation for cancer metalloimmunotherapy. J Control Release. 2024; 370: 354-366.
65. Zhang W, Cai K, Sun Z, Xiang Q, Yuan L, Fu M, et al. Elevating second near-infrared photothermal conversion efficiency of hollow gold nanorod for a precise theranostic of orthotopic bladder cancer. ACS Nano. 2023; 17: 18932-18941.
66. Zhu Z, Yang B, Wang K, Li Y, Zhu K, Gao H, et al. Ferroptosis-enhanced radiopharmaceutical therapy via a manganese-based nanoplatform. Mol Pharm. 2025; 22: 6215-6227.